nature climate change

ARTICLES

https://doi.org/10.1038/s41558-020-0781-5

Plant hydraulics accentuates the effect of atmospheric moisture stress on transpiration

Yanlan Liu[1]✉, Mukesh Kumar[2], Gabriel G. Katul[3], Xue Feng[4] and Alexandra G. Konings[1]

Transpiration, the dominant component of terrestrial evapotranspiration (ET), directly connects the water, energy and carbon cycles and is typically restricted by soil and atmospheric (for example, the vapour pressure deficit (VPD)) moisture stresses through plant hydraulic processes. These sources of stress are likely to diverge under climate change, with a globally enhanced VPD but more variable and uncertain changes in soil moisture. Here, using a model–data fusion approach, we demonstrate that the common empirical approach used in most Earth system models to evaluate the ET response to soil moisture and VPD, which neglects plant hydraulics, underestimates ET sensitivity to VPD and compensates by overestimating the sensitivity to soil moisture stress. A hydraulic model that describes water transport through the plant better captures ET under high VPD conditions for wide-ranging soil moisture states. These findings highlight the central role of plant hydraulics in regulating the increasing importance of atmospheric moisture stress on biosphere–atmosphere interactions under elevated temperatures.

ET recycles around 60% of land precipitation back to the atmosphere[1], which constrains the water resources available for human societies[2]. About 65% of ET is contributed by plant-mediated transpiration[3], which is directly linked to ecosystem productivity through stomatal conductance. Transpiration and ecosystem productivity are regulated by hydroclimatic stresses, that is, soil moisture[4,5] and the vapour pressure deficit (VPD)[6,7]. Plant responses to these stresses affect the hydrological prediction[8] and remain a dominant source of uncertainty in feedbacks between the biosphere and climate[4,5,9]. This uncertainty undermines the long-term predictability of water, carbon and energy budgets.

Soil moisture and VPD are often correlated (a lower soil moisture is often accompanied by drier air), which maks it challenging to disentangle the effects of these two stressors on ET empirically[10]. However, VPD is projected to rise globally with increased air temperature. By contrast, projected soil moisture changes are heterogeneous and uncertain[11]. As the impact of VPD on ET is likely to be amplified under elevated temperatures[10], land surface and Earth system models need to correctly account for the impact of VPD stress at wide-ranging soil moisture states.

Soil moisture and VPD, which measure the supply and demand for water, simultaneously constrain water transport through the plant. The plant vascular system delivers water extracted from the soil up to the leaves. The plant's water potential becomes more negative with increased water loss to the atmosphere. In the leaves, the extent of stomatal closure that controls the gas exchange of carbon dioxide and water vapour is also affected by leaf water potential. As leaf water potential adjusts to balance the supply and demand for water, it is intrinsically linked to VPD. Although this mechanism has been recognized for decades[12] to have profound ecological impacts[13,14], it is commonly neglected in large-scale ET estimation. Instead, independent reduction functions for each of root-zone soil moisture and VPD are used, which are empirically calibrated and assigned per plant functional type[15,16]. Over long timescales, the empirical representations are able to achieve adequate skills in capturing the observed ET[17], which motivates their wide usage in contemporary models. It remains unclear, however, whether empirical models can disentangle the ET responses to soil moisture and VPD variability. Recent studies demonstrated that incorporating plant hydraulics improves stomatal conductance and ET estimates under dry conditions[17,18], which implies misrepresented stress responses in empirical models.

Here, the responses of transpiration to soil and atmospheric moisture stresses are compared using a common empirical representation as a reference and a hydraulic representation. Accounting for plant hydraulics in ET models has been partly challenged by the scarcity of hydraulic trait measurements. This challenge is further exacerbated by large inter- and intraspecific variability in hydraulic traits[19], and the differences between in situ trait measurements that represent a particular plant segment and the effective stand-scale traits that are necessary for models[20]. To address these challenges, a model–data fusion approach was employed. This approach estimates the traits that, when combined with a given model, best match the observed temporal variation of ET. Two soil–plant water transfer models were set up using either a hydraulic representation of stomatal conductance or the more common empirical representation, with all else being the same. In both cases, the Penman–Monteith equation derived from an energy balance is used to describe ET as a function of stomatal conductance (Methods and Supplementary Note 1). Both approaches can be represented using a mathematical structure in which stomatal conductance (g_s) is reduced from a reference value by multiplicative stress functions, for example:

$$g_s = g_s^*(1 - m\ln D) \quad (1)$$

where g_s^* is the reference stomatal conductance at a VPD (D) of 1 kPa and reduces with soil or plant water status, and m is the sensitivity of stomatal conductance to VPD. For the empirical model, g_s^* reduces with decreasing soil moisture and m is held constant. As described in Methods, a stomatal-optimization based plant hydraulic model can be reformulated into the same form as equation (1) under light-saturated conditions. In that case, both g_s^* and

[1]Department of Earth System Science, Stanford University, Stanford, CA, USA. [2]Department of Civil, Construction, and Environmental Engineering, University of Alabama, Tuscaloosa, AL, USA. [3]Nicholas School of the Environment, Duke University, Durham, NC, USA. [4]Department of Civil, Environmental and Geo-Engineering, University of Minnesota, Twin Cities, MN, USA. ✉e-mail: yanlan@stanford.edu

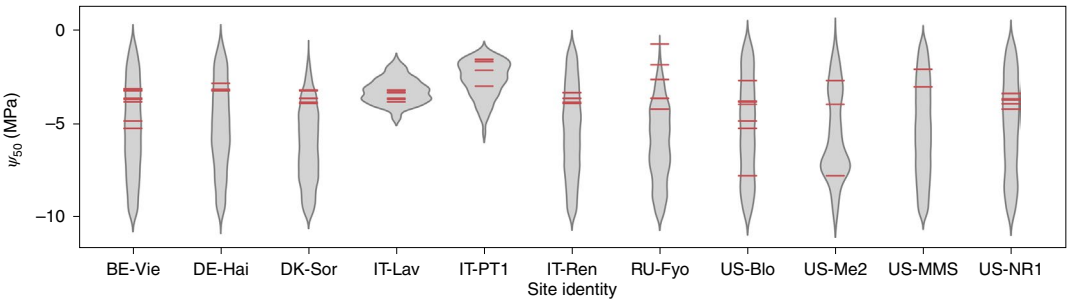

Fig. 1 | Comparison between measured and inferred ψ_{50}. Red lines denote the available ψ_{50} measurements for dominant species at sites from Anderegg et al.[13]. Grey violins represent the posterior distributions estimated using the model–data fusion approach. Site locations are listed in Supplementary Table 1.

m are functions of leaf water potential and change over time based on soil moisture and VPD[21,22]. Note that both g_s^* and m are therefore associated with different quantities in the hydraulic and empirical models (Methods). Nevertheless, the equivalent functional form in equation (1) enables the study of each model's VPD and soil moisture sensitivities. The link between m and leaf water potential can be established using a dynamic optimality theory at the leaf scale that assume leaves maximize carbon gain over a certain time interval subject to both hydrological and hydraulic constraints[23]. Both types of models were applied at 40 FLUXNET sites that covered a variety of plant functional types, climate types and stress regimes (Supplementary Table 1 and Extended Data Fig. 1). For each model, site-specific parameters, that is, empirical parameters and hydraulic traits, were retrieved using a Markov Chain Monte Carlo (MCMC) method (Methods and Supplementary Note 2). This ensures that each of the models performs optimally, and that any difference in model behaviour arises only from the model structure rather than an inappropriate parameterization of either model.

To evaluate the efficacy of model–data fusion in identifying hydraulic traits, the estimated ψ_{50} (xylem water potential at which 50% of maximum xylem conductance is lost) for a given site was compared to the available measurements for the same species (Fig. 1). As one of the most extensively measured hydraulic traits, ψ_{50} characterizes the reduction of xylem conductance (equation (8) in Methods) and the transpiration-available water under stress[14]. At most sites, the estimated ψ_{50} posterior distributions (grey areas in Fig. 1) are almost uniformly distributed, which suggests a low sensitivity of ET to ψ_{50}. This is because the leaf water potential mostly remains high and thus is rarely influenced by ψ_{50} (Extended Data Fig. 2). It is also affected by the trade-off of ψ_{50} with other hydraulic traits across MCMC samples that generate a similar ET (Extended Data Fig. 3). However, where the MCMC-inferred ψ_{50} has a narrower posterior, such as at sites IT-Lav, IT-PT1 and US-Me2, the estimated probability distribution is centred around values measured for the dominant species (red lines in Fig. 1). Other retrieved plant hydraulic traits across the studied sites are shown in Extended Data Fig. 4. For the empirical model, the average value of m across the sites is estimated as 0.58, consistent with the estimate of 0.60 obtained in a previous meta-analysis[24] and predicted from stomatal optimization theories under well-watered conditions[21]. These comparisons show that the model–data fusion approach retrieves site-specific traits that show consistency with the available independent estimates. The model performance was optimized for further analysis of model structural differences.

Across the entire study period and at each site, the hydraulic and empirical models capture daily ET with similar skills, with a coefficient of determination (R^2) that ranges from 0.12 to 0.90 and root mean square error (RMSE) from 0.31 to 1.13 mm day^{-1} across the sites (Fig. 2a,d). Notably, when focusing on subperiods of certain stress regimes, the hydraulic model improves the estimation accuracy during high VPD (higher than the 75th percentile) subperiods (Fig. 2b,e). This result is consistent with previous findings that leaf water potential improves stomatal conductance estimation during drought[17,18], although these studies did not differentiate among VPD regimes. Note that the Bayesian information criterion of the hydraulic model is consistently lower than that of the empirical model across the sites (Extended Data Fig. 5), which suggests the improved model performance due to plant hydraulics is not solely because of an additional fitting parameter in this model. Figure 2 suggests that the improvement by plant hydraulics is prominent under high VPD conditions in combination with both low (lower than the 25th percentile) and high soil moisture. By contrast, when low soil moisture conditions co-occur in combination with low VPD, there is no commensurate improvement in the performance of the hydraulic model over the empirical model (Fig. 2c,f).

To explore why the two models respond differently to high VPD conditions (Fig. 2), the degree to which VPD and soil moisture limit ET through stomatal conductance, termed the restriction effect (ΔET in Fig. 3), was evaluated for each model. It was quantified as the ratio between a benchmark ET and the modelled ET under observed stress (equations (14) and (15) in Methods). The benchmark ET was calculated using stomatal conductance under either soil moisture at the field capacity or a reference VPD of 0.6 kPa (ref. [10]). That is, the restriction effect represents the relative increase of ET in the absence of either soil moisture or VPD stresses. For most sites, the ET estimated by the hydraulic model (ET_{hydr}) is limited less by soil moisture but more by VPD than the ET of the empirical model (ET_{empr}) is (Fig. 3), and this effect is independent of site dryness (Extended Data Fig. 6). The pattern of Fig. 3 also holds when calculated for different subperiods of VPD and soil moisture (Extended Data Fig. 7). As expected, the VPD limitation of the hydraulic model is primarily accentuated under high VPD conditions and, analogously, the empirical model shows the greatest soil moisture limitation under low soil moisture conditions (Extended Data Fig. 7). This result suggests that, although both models provide a similar ET estimation on average (Fig. 2a,d), the sources of stress are distinct.

Further investigation of the underlying reason for this difference was enabled by the consistent mathematical form of g_s (equation (1)) for both models. We attribute the greater VPD restriction effect of the hydraulic model to three primary factors (calculated as in Supplementary Note 3): (1) a difference in the optimized mean m and g_s^* with respect to those of the empirical model, (2) the temporal variability (dynamics) of g_s^*, which varies in response to leaf water potential rather than to soil moisture, and (3) the dynamics of m in contrast to a constant m of the empirical model. The first factor is illustrated in Fig. 4a, which shows the optimized combinations of g_s^* and m for all sites. In the empirical model, g_s^* varies independently from m. In the hydraulic model, by contrast, reducing the leaf water

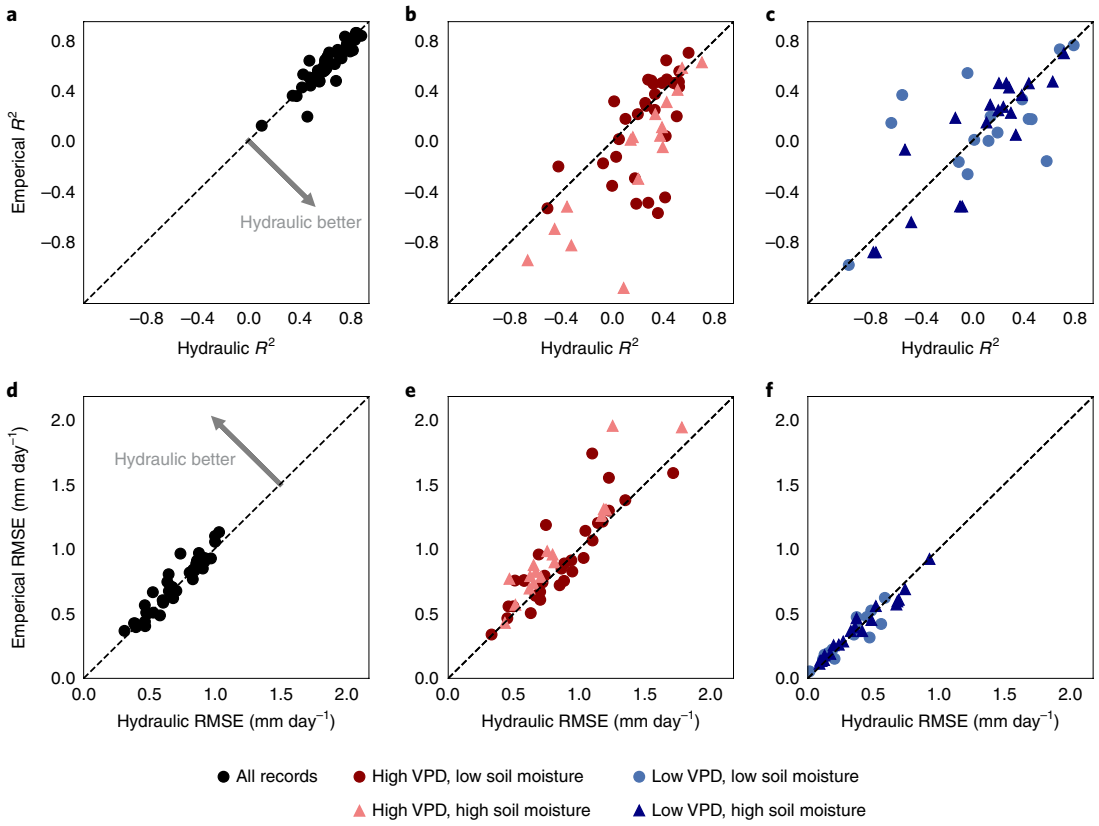

Fig. 2 | Model performance in estimating observed ET. a–f, The performances of the empirical and hydraulic models were evaluated using R^2 (**a**–**c**) and RMSE (**d**–**f**) for the all record period (**a**,**d**), subperiods with a high VPD in combination with a low or high soil moisture (**b**,**e**) and subperiods with a low VPD in combination with a low or high soil moisture (**c**,**f**). R^2 was calculated as 1 − SSR/SST, where SSR and SST are the residual sum of the squares and the total sum of squares, respectively. Negative R^2 values are caused by a biased mean of the modelled ET during the corresponding subperiods.

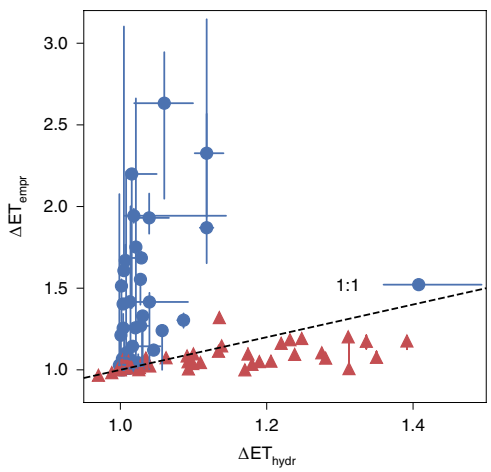

Fig. 3 | Restriction effect of hydroclimatic stresses on ET through stomatal conductance across the sites estimated using the empirical and hydraulic models. The restriction effect (ΔET) at each site is quantified as the ratio between ET modelled using stomatal conductance under a reference condition and ET modelled under observed hydroclimatic conditions. For soil-moisture-restricted ET (blue dots), the reference condition is soil moisture at the field capacity, with all else being the same. For the restriction effect of VPD on ET (red triangles), the reference condition is VPD = 0.6 kPa, with all else being the same. Vertical and horizontal lines are plotted for all sites, and denote the 25–75% uncertainty ranges due to the uncertainty in site-specific traits after MCMC.

potential under stressed conditions leads to a simultaneous decrease in g_s^* and increase in m (Methods). Thus, g_s^* and m are coupled via a hydraulic constraint that delineates a feasible region in the g_s^*–m space (Fig. 4a, light and dark grey shaded areas). Note that the exact constraint varies in time and by site (Extended Data Fig. 8). This constraint promotes a trade-off between soil moisture and VPD stresses that results in a greater mean VPD sensitivity (greater $\bar{m}$, red dots in Fig. 4a) compared with that in the empirical model. This difference in mean contributes 45% of ΔET_{hydr}^{VPD} averaged across the sites (Extended Data Fig. 9). Aside from the difference in mean, the temporal variations of g_s^* and m differ between the empirical and hydraulic models. In the hydraulic model, under stressed conditions g_s^* decreases and m increases with the marginal water-use efficiency as the leaf water potential drops (Methods and Extended Data Fig. 10)[21,22]. These magnify the restriction effect of VPD on ET. The difference between the static m for the empirical model and the dynamic m for the hydraulic model is illustrated in Fig. 4b. The median value of m increases by 51% under the most stressed conditions. Across the sites, the dynamics of g_s^* and m have impacts on ΔET_{hydr}^{VPD} that are 87 and 8%, respectively, as large as those of the dominant factor, that is, the difference in means. Nevertheless, the dynamics of m becomes more important under stressed conditions, and account for a 28% increase to that of the difference in means (Extended Data Fig. 9).

The above comparison between model structures was enabled by the model–data fusion approach, which resolves parameter uncertainty by identifying optimal parameters and their uncertainty. The analysis here illustrates that in the presence of soil moisture–VPD correlation, the current generation of stomatal conductance models compensate between VPD and soil moisture sensitivities (Figs. 3 and 4).

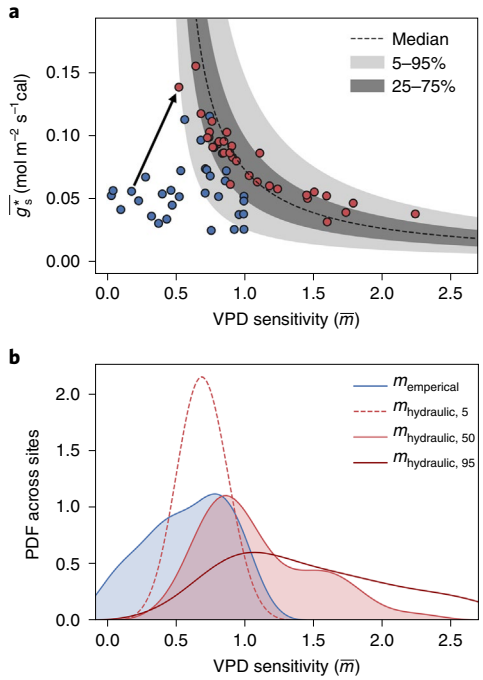

Fig. 4 | Reference stomatal conductance and VPD sensitivity estimated using the empirical and hydraulic models. a, The temporal averages of the reference stomatal conductance ($\overline{g_s^*}$) and the VPD sensitivity ($\bar{m}$) from the empirical (blue dots) and hydraulic (red dots) models across the sites. The black dashed line and grey shaded areas show the median and percentile ranges of the hydraulic constraint that couples g_s^* and m (red dots) across all times and all sites. **b**, The probability distribution functions (PDFs) of the VPD sensitivity across the sites estimated using the empirical (m_{empr}, blue PDF) and hydraulic (m_{hydr}, red PDFs under a range of stressed conditions) models. $m_{hydr,5}$, $m_{hydr,50}$ and $m_{hydr,95}$ denote the 5th, 50th and 95th percentiles, respectively. Only data under light-saturated conditions were used to calculate g_s^* and m of the hydraulic model, and only sites with light-saturated conditions for longer than 100 h are plotted.

Note that uncertainties exist in the hydraulic model, which include a lack of representation of plant water storage and embolism propagation[25], using time-invariant vulnerability curves without accounting for dynamic embolism refilling and the growth of new xylem[26], and the assumption of constant rooting structure and biomass[27]. These factors introduce 'legacy effects' on the transpiration response to hydroclimatic stresses. Uncertainties also exist in the site-specific properties used to parameterize the model (Supplementary Table 1), although sensitivity analysis suggests that the main results are qualitatively robust with respect to rooting depth, a key parameter that affects plant water uptake (Supplementary Figs. 2 and 3). Nevertheless, as the compensating errors in the empirical model are induced by its structure, which is shared by most large-scale models without plant hydraulics[15,16], the qualitative results found here are expected to be robust.

Our findings highlight a stronger impact of atmospheric moisture stress on ecosystem transpiration than that commonly represented in land surface models due to the effects of plant hydraulics. The current generation of models therefore probably underestimates the future impairment of ecosystem productivity and biosphere–atmosphere interactions by elevated temperatures. They also probably overestimate the reduction in water resources during warmer droughts. As such, there is a need to incorporate plant hydraulics in the next generation of Earth system models. This need is already recognized, as doing so improves the predictions of plant vulnerability under droughts[28]. The mechanistic nature of plant hydraulic models may also facilitate accounting for changes of plant traits under climate change. Although plant hydraulic representations are slowly becoming more common in large-scale models[29,30], the impact of such changing representations on ecosystem flux predictions remains understudied, and the majority of large-scale models still neglect plant hydraulics. However, as such representations become more widespread, parameterizing the traits will remain a key challenge. The model–data fusion approach used here points to the possibility of tackling this challenge by integrating models with large-scale observations. Doing so will improve the prediction of ecosystems and water resources under future droughts.

Online content

Any methods, additional references, Nature Research reporting summaries, source data, extended data, supplementary information, acknowledgements, peer review information; details of author contributions and competing interests; and statements of data and code availability are available at https://doi.org/10.1038/s41558-020-0781-5.

Received: 24 October 2019; Accepted: 15 April 2020;
Published online: 01 June 2020

References

1. Oki, T. & Kanae, S. Global hydrological cycles and world water resources. *Science* **313**, 1068–1072 (2006).
2. Seager, R. et al. Projections of declining surface-water availability for the southwestern United States. *Nat. Clim. Change* **3**, 482–486 (2013).
3. Good, S. P., Noone, D. & Bowen, G. Hydrologic connectivity constrains partitioning of global terrestrial water fluxes. *Science* **349**, 175–177 (2015).
4. Trugman, A., Medvigy, D., Mankin, J. & Anderegg, W. Soil moisture stress as a major driver of carbon cycle uncertainty. *Geophys. Res. Lett.* **45**, 6495–6503 (2018).
5. Green, J. K. et al. Large influence of soil moisture on long-term terrestrial carbon uptake. *Nature* **565**, 476–479 (2019).
6. Konings, A., Williams, A. & Gentine, P. Sensitivity of grassland productivity to aridity controlled by stomatal and xylem regulation. *Nat. Geosci.* **10**, 284–289 (2017).
7. Rigden, A. J. & Salvucci, G. D. Stomatal response to humidity and CO_2 implicated in recent decline in US evaporation. *Global Change Biol.* **23**, 1140–1151 (2017).
8. Mirfenderesgi, G. et al. Tree level hydrodynamic approach for resolving aboveground water storage and stomatal conductance and modeling the effects of tree hydraulic strategy. *J. Geophys. Res. Biogeosci.* **121**, 1792–1813 (2016).
9. Reichstein, M. et al. Climate extremes and the carbon cycle. *Nature* **500**, 287–295 (2013).
10. Novick, K. A. et al. The increasing importance of atmospheric demand for ecosystem water and carbon fluxes. *Nat. Clim. Change* **6**, 1023–1027 (2016).
11. IPCC *Climate Change 2013: The Physical Science Basis* (eds Stocker, T. F. et al.) (Cambridge Univ. Press, 2013).
12. Tyree, M. T. & Sperry, J. S. Vulnerability of xylem to cavitation and embolism. *Ann. Rev. Plant Biol.* **40**, 19–36 (1989).
13. Anderegg, W. R. et al. Hydraulic diversity of forests regulates ecosystem resilience during drought. *Nature* **561**, 538–541 (2018).
14. Feng, X., Dawson, T. E., Ackerly, D. D., Santiago, L. S. & Thompson, S. E. Reconciling seasonal hydraulic risk and plant water use through probabilistic soil–plant dynamics. *Global Change Biol.* **23**, 3758–3769 (2017).
15. Oleson, K. W. et al. *Technical Description of Version 4.5 of the Community Land Model (CLM)* NCAR Technical Note NCAR/TN-503+STR (National Center for Atmospheric Research, 2013).
16. Milly, P. C. et al. An enhanced model of land water and energy for global hydrologic and earth-system studies. *J. Hydrometeorol.* **15**, 1739–1761 (2014).
17. Bonan, G., Williams, M., Fisher, R. & Oleson, K. Modeling stomatal conductance in the earth system: linking leaf water-use efficiency and water transport along the soil–plant–atmosphere continuum. *Geosci. Model Dev.* **7**, 2193–2222 (2014).
18. Anderegg, W. R. et al. Plant water potential improves prediction of empirical stomatal models. *PloS ONE* **12**, e0185481 (2017).
19. Anderegg, W. R. Spatial and temporal variation in plant hydraulic traits and their relevance for climate change impacts on vegetation. *New Phytol.* **205**, 1008–1014 (2015).
20. Meinzer, F. C., McCulloh, K. A., Lachenbruch, B., Woodruff, D. R. & Johnson, D. M. The blind men and the elephant: the impact of context and scale in evaluating conflicts between plant hydraulic safety and efficiency. *Oecologia* **164**, 287–296 (2010).

21. Katul, G. G., Palmroth, S. & Oren, R. Leaf stomatal responses to vapour pressure deficit under current and CO_2-enriched atmosphere explained by the economics of gas exchange. *Plant Cell Environ.* **32**, 968–979 (2009).
22. Manzoni, S. et al. Optimizing stomatal conductance for maximum carbon gain under water stress: a meta-analysis across plant functional types and climates. *Funct. Ecol.* **25**, 456–467 (2011).
23. Mrad, A. et al. A dynamic optimality principle for water use strategies explains isohydric to anisohydric plant responses to drought. *Front. For. Global Change* **2**, 49 (2019).
24. Oren, R. et al. Survey and synthesis of intra- and interspecific variation in stomatal sensitivity to vapour pressure deficit. *Plant Cell Environ.* **22**, 1515–1526 (1999).
25. Mrad, A., Domec, J.-C., Huang, C.-W., Lens, F. & Katul, G. A network model links wood anatomy to xylem tissue hydraulic behaviour and vulnerability to cavitation. *Plant Cell Environ.* **41**, 2718–2730 (2018).
26. Venturas, M. D., Sperry, J. S. & Hacke, U. G. Plant xylem hydraulics: what we understand, current research, and future challenges. *J. Integr. Plant Biol.* **59**, 356–389 (2017).
27. Doughty, C. E. et al. Drought impact on forest carbon dynamics and fluxes in Amazonia. *Nature* **519**, 78–82 (2015).
28. Fisher, R. A. et al. Vegetation demographics in Earth system models: a review of progress and priorities. *Global Change Biol.* **24**, 35–54 (2018).
29. Eller, C. B. et al. Modelling tropical forest responses to drought and El Niño with a stomatal optimization model based on xylem hydraulics. *Phil. Trans. R. Soc. B* **373**, 20170315 (2018).
30. Kennedy, D. et al. Implementing plant hydraulics in the community land model, version 5. *J. Adv. Model. Earth Syst.* **11**, 485–513 (2019).

Methods

Soil–plant model. The soil–plant model is described in Liu et al.[31]. Evaporation and transpiration are calculated based on energy balance on the ground and canopy surfaces (Supplementary Note 1). Transpiration (E_l) is a function of stomatal conductance (g_s), which is computed using either an empirical a hydraulic representation.

In the empirical representation:

$$g_s = g^*_{s,empr}(1 - m_{empr} \ln D) \quad (2)$$

where the VPD sensitivity m_{empr} is held constant and the reference stomatal conductance $g^*_{s,empr}$ is restricted by the root-zone soil moisture[15], that is:

$$g^*_{s,empr} = g_{s,ref} \sum_{i=1}^{N_l} r(i) \max\left[0, \min\left(\frac{\theta_i - \theta_w}{\theta_s - \theta_w}, 1\right)\right] \quad (3)$$

where $g_{s,ref}$ is the maximum $g^*_{s,ref}$; N_l is the total number of layers for the soil column from the ground surface to the maximum rooting depth (Z_r). Here, $N_l = 2$ with the two layers separated at 0.3 m if $Z_r > 0.3$ m, and $N_l = 1$ otherwise. $r(i)$ is the fraction of roots in layer i. θ_s and θ_w are the stress thresholds when the soil moisture stress commences and when the stomata fully close, respectively. θ_i is the volumetric soil moisture in layer i. As few FLUXNET sites report soil moisture below 0.3 m, for $N_l = 2$, θ_2 is modelled based on water balance, that is:

$$Z_{r,2} \frac{d\theta_2}{dt} = L_{1,2} - L_{2,3} - E_{l,2} \quad (4)$$

where $Z_{r,2}$ is the thickness of the second layer; $L_{1,2}$ and $L_{2,3}$ are the leakage from the first to the second layer and out of the rooting zone, respectively, which are calculated from Darcy's law as described elsewhere[31]. A boundary condition of constant water content (θ_{bc}) below the rooting zone is assumed for the $L_{2,3}$ calculation. $E_{l,2}$ is the plant water uptake from the second layer, modelled as $E_{l,2} = r(2)E_l$ following Oleson et al.[15].

In the hydraulic model, the stomatal conductance is computed using the leaf-gas exchange optimality theory[32], that is:

$$g_s = \text{argmax} f_c(g_s) - \lambda f_e(g_s) \quad (5)$$

where $f_c(g_s)$ and $f_e(g_s)$ are the carbon gain and water loss, respectively, following Fickian diffusion; λ is the marginal water use efficiency that describes the cost of loosing water in carbon units. As described elsewhere[31], g_s can be solved under a given λ by combining equation (5) with the biochemical demand for CO_2 (ref. [33]). λ has been shown to respond to leaf water potential (ψ_l) (ref. [22]), that is:

$$\lambda = \lambda_W \exp(\beta_0 \overline{\psi_l}) \quad (6)$$

where λ_W is the marginal water use efficiency under the ambient CO_2 concentration and well-watered conditions, β_0 is the sensitivity parameter and $\overline{\psi_l}$ is ψ_l averaged over the previous 24 h (refs. [22,34]). λ depends on $\overline{\psi_l}$ on a daily timescale rather than the instant ψ_l based on theoretical and observational studies, which suggests that λ varies at a longer timescale than g_s and could evolve with soil water availability[22,23,32,35–37]. ψ_l controls water supply through the plant hydraulic system, which is solved by equating the supply to the demand determined by energy balance (Supplementary Note 1) according to the continuity assumption[38]:

$$E_l = \int_{\psi_r}^{\psi_l} g_p(x)\, dx \quad (7)$$

where ψ_r is the root water potential and g_p is the whole-plant xylem conductance, which follows a vulnerability curve[39]:

$$g_p(x) = g_{p,max}\left[1 + \left(\frac{x}{\psi_{50}}\right)^a\right]^{-1} \quad (8)$$

where $g_{p,max}$ is the maximum whole-plant xylem conductance and a is the curvature parameter of the vulnerability curve. The soil layer characterization is the same as that in the empirical representation. For sites where $N_l = 2$, the same water balance model (equation (4)) is used to model the second layer soil moisture. Here, $E_{l,2}$ is calculated using a resistance-based approach based on soil and root water potentials and the soil–root conductance[31]. The soil water potential is obtained based on soil texture and moisture content[40], and the soil–root conductance is calculated using a cylinder root model that depends on the root depth, root area index and soil hydraulic conductivity[41].

Next, the mathematical connection between the hydraulic representation and the empirical representation is described. Under light-saturated conditions, the solution of equation (5) can be linearized as[32]:

$$g_s = \alpha\left[-1 + \left(\frac{c_a}{a_0 \lambda}\right)^{1/2} D^{-1/2}\right] \quad (9)$$

where α contains parameters describing the biochemical demand for CO_2 (ref. [33]), c_a is atmospheric CO_2 concentration and $a_0 = 1.6$ is the relative diffusivity of water vapour with respect to CO_2. Denoting:

$$\Phi = \left(\frac{c_a}{a_0 \lambda}\right)^{1/2} \quad (10)$$

equation (9) can be rearranged into the following form similar to equation (2)[21]:

$$g_s = g^*_{s,hydr}(1 - m_{hydr} \ln D) \quad (11)$$

where

$$g^*_{s,hydr} = \alpha(-1 + \Phi) \quad (12)$$

$$m_{hydr} = \frac{1}{2}\frac{\Phi}{\Phi - 1} k_D \quad (13)$$

in which $k_D = 2(1 - D^{-1/2})/\ln D$. Based on a Taylor series expansion, $D^{-1/2} = 1 - (1/2)\ln D + O((\ln D)^2)D^{-1/2}$. Therefore $k_D \approx 1$ when $D \approx 1$ kPa, that is, k_D is the correction factor of the Taylor series approximation when D deviates from 1 kPa. It can be seen that $g^*_{s,hydr}$ and m_{hydr} are coupled through λ and thus leaf water potential. That is, as soil water is diminished, the cost of loosing water (in carbon units) to the plant increases, which results in an increased λ.

Datasets and site properties. The soil–plant model was applied at 40 sites in the FLUXNET2015 dataset[42] across the globe, which covers a range of climate and land-cover types (Supplementary Table 1). Sites were chosen to ensure that soil moisture, net radiation, air temperature, humidity, precipitation, sensible and latent heat fluxes, wind speed and friction velocity were collected half-hourly or hourly for at least two years. Sites covered by savanna were excluded from the analysis due to the large spatial heterogeneity in vegetation cover. For each site, daytime measurements on days with no precipitation and daily minimum temperatures higher than 0 °C during the growing season were used as the study period to estimate plant traits and evaluate the model performance. April to October and November to March was considered as the growing season for sites in the Northern Hemisphere and Sourthern Hemisphere, respectively, except for evergreen broadleaf sites, where the growing season spans over the entire year. No groundwater access at these sites was documented in the literature listed in the FLUXNET2015 dataset information[42]. The site and data-filtering criteria helped reduce uncertainties introduced by a large soil evaporation, understory species, snow cover, frozen soil and groundwater access.

The leaf area index at each site was extracted from the MODIS (Moderate Resolution Imaging Spectroradiometer) product (MCD15A3H.006) with a spatial and temporal resolution of 500 m and 4 days[43] using the Google Earth Engine and was linearly interpolated to the same temporal resolution as the flux measurements. Canopy and measurement heights were obtained from site-specific information[44] or, if no site-specific information was available, the GLAS (Geoscience Laser Altimeter System) canopy height dataset[45]. Maximum rooting depth (Z_r) was obtained from the literature (Supplementary Table 1) or, if not available, a synthesized global map[46]. The rooting profile across the layers ($r(i)$) was calculated as a function of depth using the shape function in Jackson et al.[47], in which the total root area index and the distribution parameter were specified for each biome based on plant functional type and climate type[48]. Soil texture was obtained from the literature for each site (Supplementary Table 1) or extracted from the Harmonized World Soils Database[49] if no information was available in the literature.

Model–data fusion using MCMC. Except for the described site-specific characteristics, a majority of the traits related to the soil–plant hydraulic system were systematically retrieved using a MCMC method to identify the most likely set of traits that leads to model outputs consistent with the observed ET at each site. In the empirical representation, the plant traits include $g_{s,ref}$, m_{empr}, θ_w and θ_s (equations (2) and (3)), and λ_W, β_0, $g_{p,max}$, ψ_{50} and a are the plant hydraulic traits used in the hydraulic representation (equations (6) and (8)). The soil parameters include the shape parameter of the soil water retention curve[40] and θ_{bc} to account for uncertain subsurface hydrological conditions[50]. MCMC requires prior knowledge on the probability distribution of the target parameters. For the hydraulic representation, a flat prior distribution that spanned the possible range of each hydraulic trait based on meta-analyses[22,51] was provided, that is, $(0, 10{,}000)$ μmol mol^{-1} for λ_W, $(-2, 0)$ MPa^{-1} for β_0, $(10^{-9}, 10^{-5})$ m s^{-1} MPa^{-1} for $g_{p,max}$ (flat in a log scale), $(-10, 0)$ MPa for ψ_{50} and $(0, 8)$ for a. In addition to the prior ranges, physiological constraints from meta-analysis[18,52] were also incorporated to avoid unrealistic combinations of hydraulic traits that nevertheless match data (Supplementary Note 2). For the empirical representation, based on the range of estimates in previous studies[10,24], uniform priors of $(0, 1)$ mol m^{-2} s^{-1} and $(0, 1)$ ln(kPa)$^{-1}$ were used for $g_{s,ref}$ and m_{empr}, respectively. A uniform distribution between the soil water content that corresponded to a soil water potential of −10 MPa and the full saturation was used as the prior for θ_w, θ_s and θ_{bc}. A Gaussian prior was used for the shape

parameter of the soil water retention curve, with the mean and standard deviation from multisample measurements[40] for the corresponding soil texture at each site.

Among all the collected data at each site, observations in a normal year and a dry year were chosen for use in the parameter retrieval to provide sufficient samples under both normal and stressed conditions. Here, a normal year had an average soil moisture and VPD within the growing season between the 25th and 75th percentiles for a given site; and a dry year had soil moisture below the 25th percentile and VPD higher than the 75th percentile. The difference between each pair of modelled and observed daily average ET representing the daily error was treated as independent and identically distributed, following a Gaussian distribution with zero mean and an unknown variance also estimated using MCMC. Thus conditional on a given set of parameters, the likelihood of observations can be computed and then used to sample the next generation of parameters. Each MCMC chain started randomly within the prior range and explored the parameter space following the Adaptive Metropolized Independence Sampling method with parallel tempering[53], generating 20,000 samples. Twenty independent MCMC chains were used for each site. Within- and among-chain convergences were diagnosed by the Geweke and Gelman–Rubin values[54]. The converged MCMC chains, after 5,000 steps for the empirical representation and 12,000 steps for the hydraulic representation, provided the estimation of the joint distribution of the target parameters. For evaluation of the model performance and the impact of hydroclimatic stresses, 100 sets of the target parameters were randomly selected from the converged joint distribution to model ET using the empirical and hydraulic representations, respectively.

Assessment of model behaviours. The accuracy of the modelled ET using the empirical and the hydraulic representations was evaluated using the coefficient of determination (R^2) for the entire study period at each site and for four subperiods with different combinations of soil moisture and VPD stress. The four subperiods included days with high or low VPD in combination with high or low soil moisture. Days with high or low VPD were identified based on the daily VPD being higher or lower than its 75th or 25th, respectively, percentile at a given site, and likewise for soil moisture. To further investigate the response of each model to different types of hydroclimatic stress, the degree to which each type of stressor limits the modelled ET was evaluated. A benchmark stomatal conductance without soil moisture (VPD) limitation was calculated under a reference condition of soil moisture at the field capacity θ_0 (VPD being $D_0 = 0.6$ kPa following Novick et al.[10]) at all times, with all else being the same. The restriction effect of soil moisture (ΔET^{θ}) and VPD (ΔET^{VPD}) on ET were then calculated per site as the ratio between the corresponding benchmark ET to the ET calculated under observed stresses, that is:

$$\Delta ET^{\theta} = \frac{ET[g_s(\theta = \theta_0, D)]}{ET[g_s(\theta, D)]} \quad (14)$$

$$\Delta ET^{VPD} = \frac{ET[g_s(\theta, D = D_0)]}{ET[g_s(\theta, D)]} \quad (15)$$

Data availability

All datasets used in this study are publicly available from the referenced sources.

Code availability

The source code of the soil-plant model and the used MCMC algorithm is available at https://github.com/YanlanLiu/model-data-fusion.

References

31. Liu, Y. et al. Increasing atmospheric humidity and CO_2 concentration alleviate forest mortality risk. *Proc. Natl Acad. Sci. USA* **114**, 9918–9923 (2017).
32. Katul, G., Manzoni, S., Palmroth, S. & Oren, R. A stomatal optimization theory to describe the effects of atmospheric CO_2 on leaf photosynthesis and transpiration. *Ann. Bot.* **105**, 431–442 (2009).
33. Farquhar, G. D., Caemmerer, S. V. & Berry, J. A. A biochemical model of photosynthetic CO_2 assimilation in leaves of C_3 species. *Planta* **149**, 78–90 (1980).
34. Huang, C.-W. et al. The effect of plant water storage on water fluxes within the coupled soil–plant system. *New Phytol.* **213**, 1093–1106 (2017).
35. Cowan, I. & Farquhar, G. Stomatal function in relation to leaf metabolism and environment. *Symp. Soc. Exp. Biol.* **31**, 471–505 (1977).
36. Hari, P., Mäkelä, A., Korpilahti, E. & Holmberg, M. Optimal control of gas exchange. *Tree Physiol.* **2**, 169–175 (1986).
37. Medlyn, B. E. et al. Reconciling the optimal and empirical approaches to modelling stomatal conductance. *Global Change Biol.* **17**, 2134–2144 (2011).
38. Sperry, J. S. et al. Predicting stomatal responses to the environment from the optimization of photosynthetic gain and hydraulic cost. *Plant Cell Environ.* **40**, 816–830 (2017).
39. Manzoni, S., Vico, G., Porporato, A. & Katul, G. Biological constraints on water transport in the soil–plant–atmosphere system. *Adv. Water Resourc.* **51**, 292–304 (2013).
40. Clapp, R. B. & Hornberger, G. M. Empirical equations for some soil hydraulic properties. *Water Resourc. Res.* **14**, 601–604 (1978).
41. Katul, G., Leuning, R. & Oren, R. Relationship between plant hydraulic and biochemical properties derived from a steady–state coupled water and carbon transport model. *Plant Cell Environ.* **26**, 339–350 (2003).
42. *FLUXNET 2015 Tier 1 Dataset* (FLUXNET, accessed 25 July 2018); http://fluxnet.fluxdata.org/data/fluxnet2015-dataset
43. Myneni, R., Knyazikhin, Y. & Park, T. *MCD15A3H MODIS/Terra+Aqua Leaf Area Index/FPAR 4-day L4 Global 500 m SIN Grid V006* (NASA EOSDIS Land Processes DAAC, accessed 21 January 2019); https://doi.org/10.5067/MODIS/MCD15A3H.006
44. Ukkola, A. M., Haughton, N., Kauwe, M. G. D., Abramowitz, G. & Pitman, A. J. FluxnetLSM R package (v1. 0): a community tool for processing FLUXNET data for use in land surface modelling. *Geosci. Model Develop.* **10**, 3379–3390 (2017).
45. Healey, S. et al. *CMS: GLAS LiDAR-derived Global Estimates of Forest Canopy Height, 2004–2008* (ORNL DAAC, accessed 21 January 2019); https://doi.org/10.3334/ORNLDAAC/1271
46. Fan, Y., Miguez-Macho, G., Jobbágy, E. G., Jackson, R. B. & Otero-Casal, C. Hydrologic regulation of plant rooting depth. *Proc. Natl Acad. Sci. USA* **114**, 10572–10577 (2017).
47. Jackson, R. et al. A global analysis of root distributions for terrestrial biomes. *Oecologia* **108**, 389–411 (1996).
48. Kottek, M., Grieser, J., Beck, C., Rudolf, B. & Rubel, F. World map of the Köppen–Geiger climate classification updated. *Meteorol. Z.* **15**, 259–263 (2006).
49. *Harmonized World Soil Database Version 1.2* (FAO, accessed 22 June 2016); http://www.fao.org/soils-portal
50. Thompson, S. E. et al. Comparative hydrology across AmeriFlux sites: the variable roles of climate, vegetation, and groundwater. *Water Resourc. Res.* **47**, W00J07 (2011).
51. Kattge, J. et al. TRY—a global database of plant traits. *Global Change Biol.* **17**, 2905–2935 (2011).
52. Martin-StPaul, N., Delzon, S. & Cochard, H. Plant resistance to drought depends on timely stomatal closure. *Ecol. Lett.* **20**, 1437–1447 (2017).
53. Ji, C. & Schmidler, S. C. Adaptive Markov Chain Monte Carlo for Bayesian variable selection. *J. Comput. Graph. Stat.* **22**, 708–728 (2013).
54. Brooks, S. P. & Gelman, A. General methods for monitoring convergence of iterative simulations. *J. Graph. Stat.* **7**, 434–455 (1998).

Acknowledgements

We acknowledge S. C. Schmidler for providing suggestions on statistical inference. A.G.K. and Y.L. were funded by NASA Terrestrial Ecology (award 80NSSC18K0715) through the New Investigator programme. A.G.K. was also funded by the NOAA under grant NA17OAR4310127. M.K. acknowledges support from the National Science Foundation (NSF, EAR-1856054 and EAR-1920425). G.G.K. acknowledges support from the National Science Foundation (NSF-AGS-1644382 and NSF-IOS-1754893).

Author contributions

A.G.K. and Y.L. conceived the study. Y.L. prepared data, set up the model and conducted statistical inference, with all the authors providing input. M.K. and G.K. further improved the analysis design. Y.L., M.K. and A.G.K. led the manuscript writing. All the authors contributed to editing the manuscript.

Competing interests

The authors declare no competing interests.

Additional information

Extended data is available for this paper at https://doi.org/10.1038/s41558-020-0781-5.

Supplementary information is available for this paper at https://doi.org/10.1038/s41558-020-0781-5.

Correspondence and requests for materials should be addressed to Y.L.

Peer review information *Nature Climate Change* thanks Maurizio Mencuccini and the other, anonymous, reviewer(s) for their contribution to the peer review of this work.

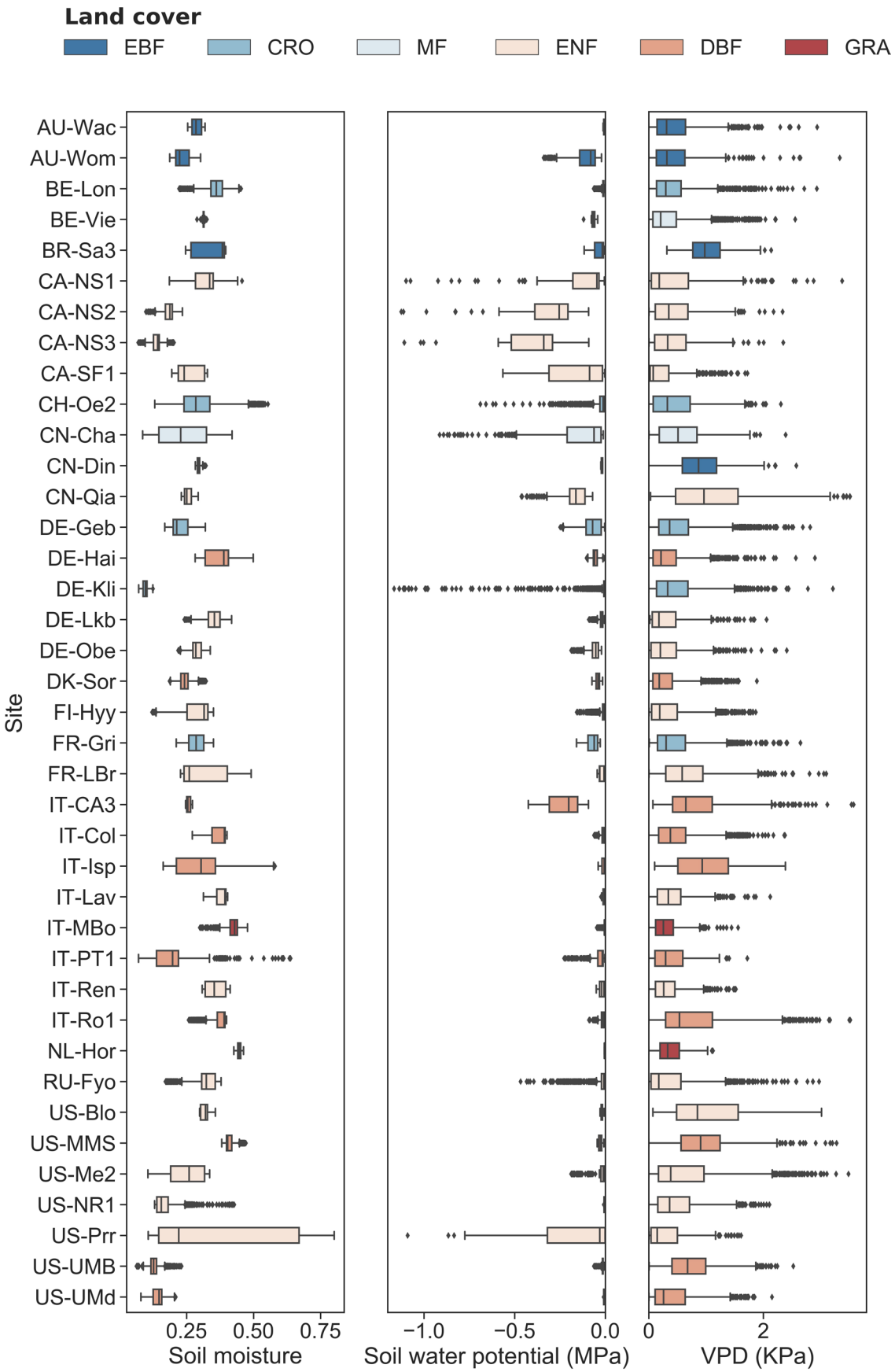

Extended Data Fig. 1 | Root zone soil moisture, soil water potential, and VPD across studied sites. Each box represents the 25th and 75th percentiles and the range across the entire record period. Outliers are marked using black dots.

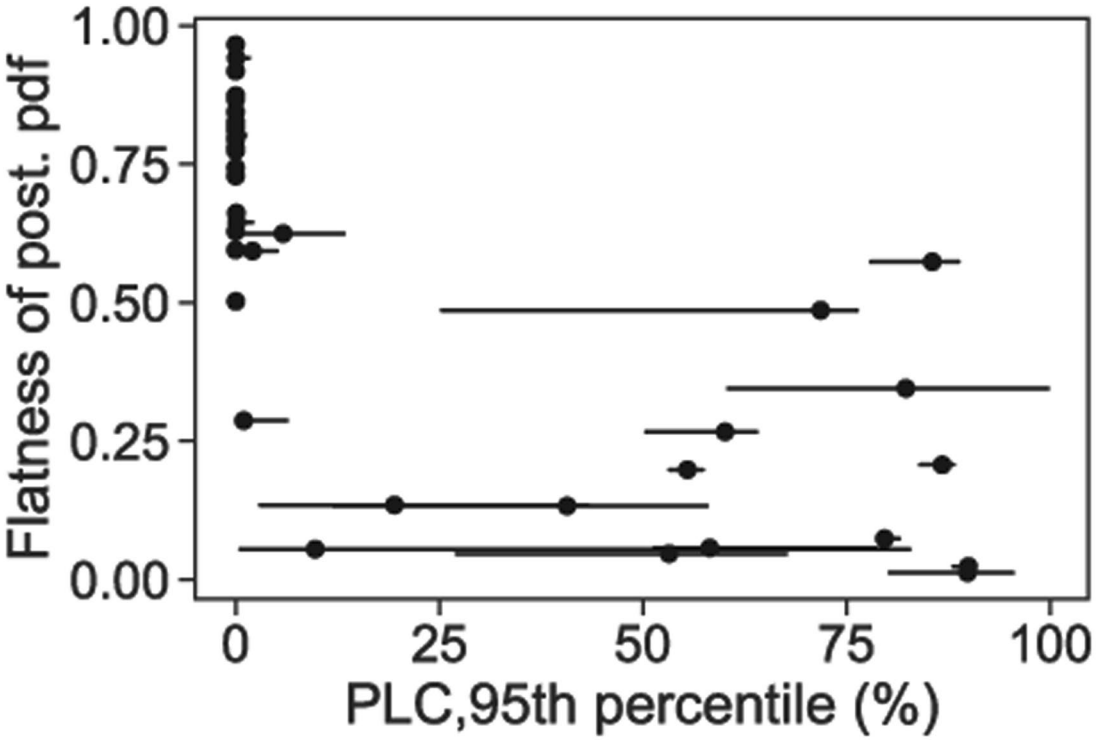

Extended Data Fig. 2 | Relation between the 95th percentile of the percentage loss of conductivity (PLC) and the flatness of posterior probability distribution of ψ_{50} across the studied sites. The flatness is quantified as $(q_{75} - q_{25})/(p_{75} - p_{25})$, where q_{75} and q_{25} are the 75th and 25th percentiles of the posterior distribution, and p_{75} and p_{25} are the 75th and 25th percentiles of the prior distribution. A flatness of 0 indicates concentrated posterior and a flatness of 1 indicates a nearly uniformly distributed posterior. Horizontal bars represent the uncertainty ranges across posterior samples.

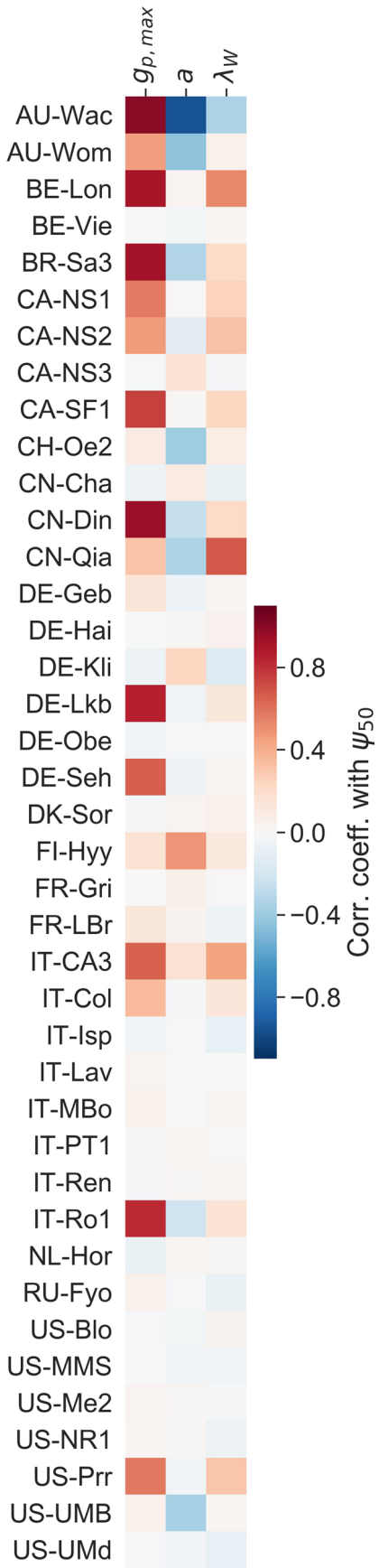

Extended Data Fig. 3 | Correlation coefficient of ψ_{50} (MPa) with $g_{p,max}$, a, and λ_W across posterior samples at the studied sites. Site information is listed in Supplementary Table 1.

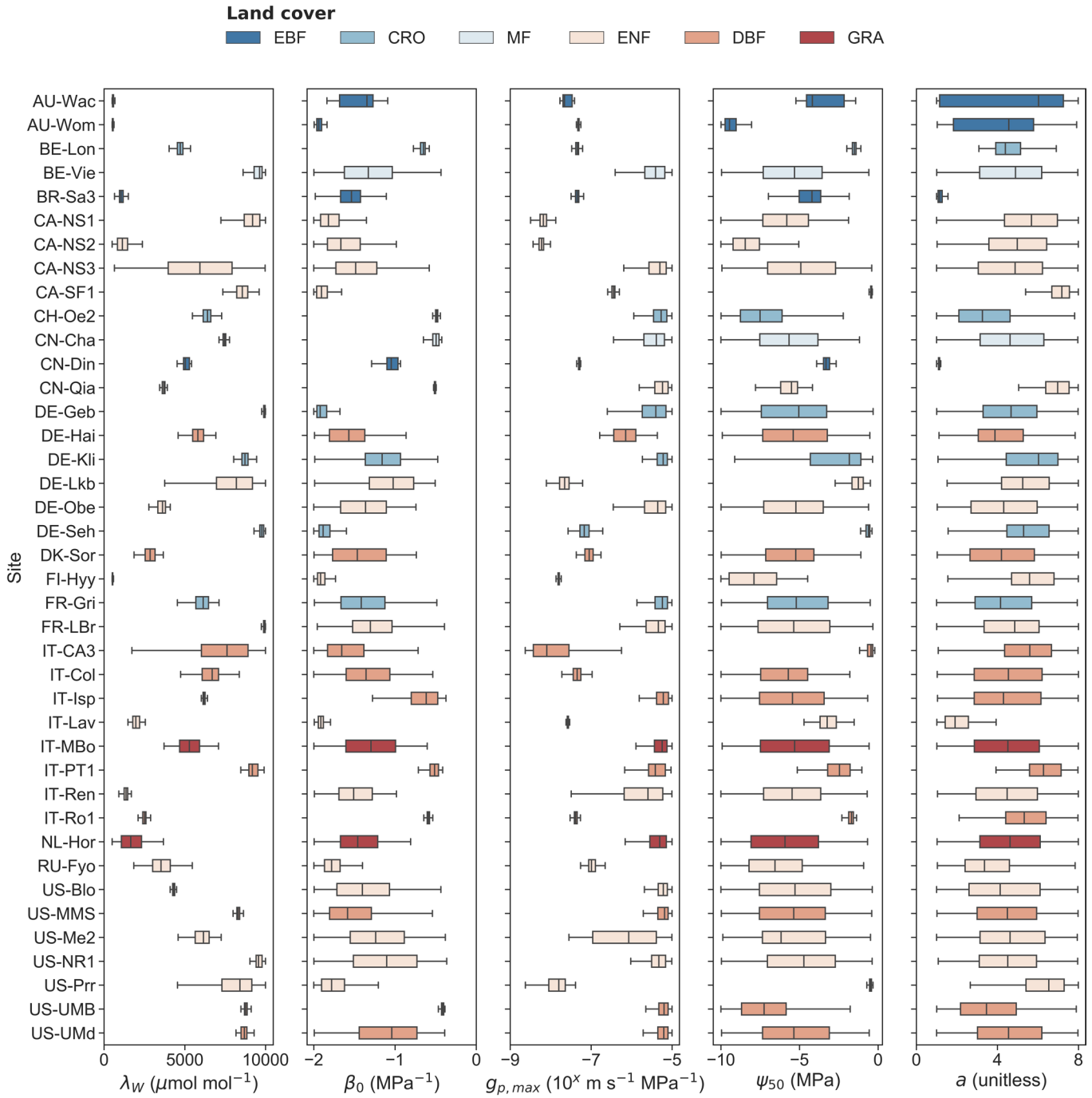

Extended Data Fig. 4 | Posterior distributions of retrieved plant hydraulic traits across studied sites. Each box denotes the 25th/75th percentiles and the range of posterior samples.

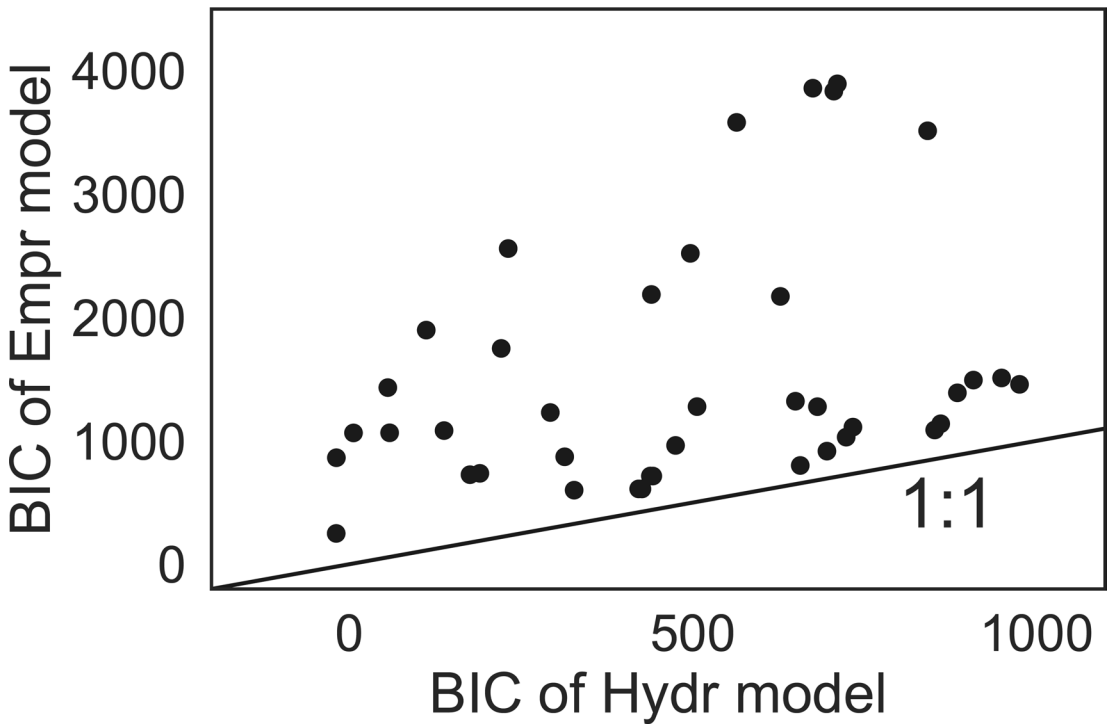

Extended Data Fig. 5 | Bayesian Information Criterion (BIC) of the hydraulic and empirical models across the studied sites. Model likelihood averaged across MCMC ensembles at each site was used to calculate BIC.

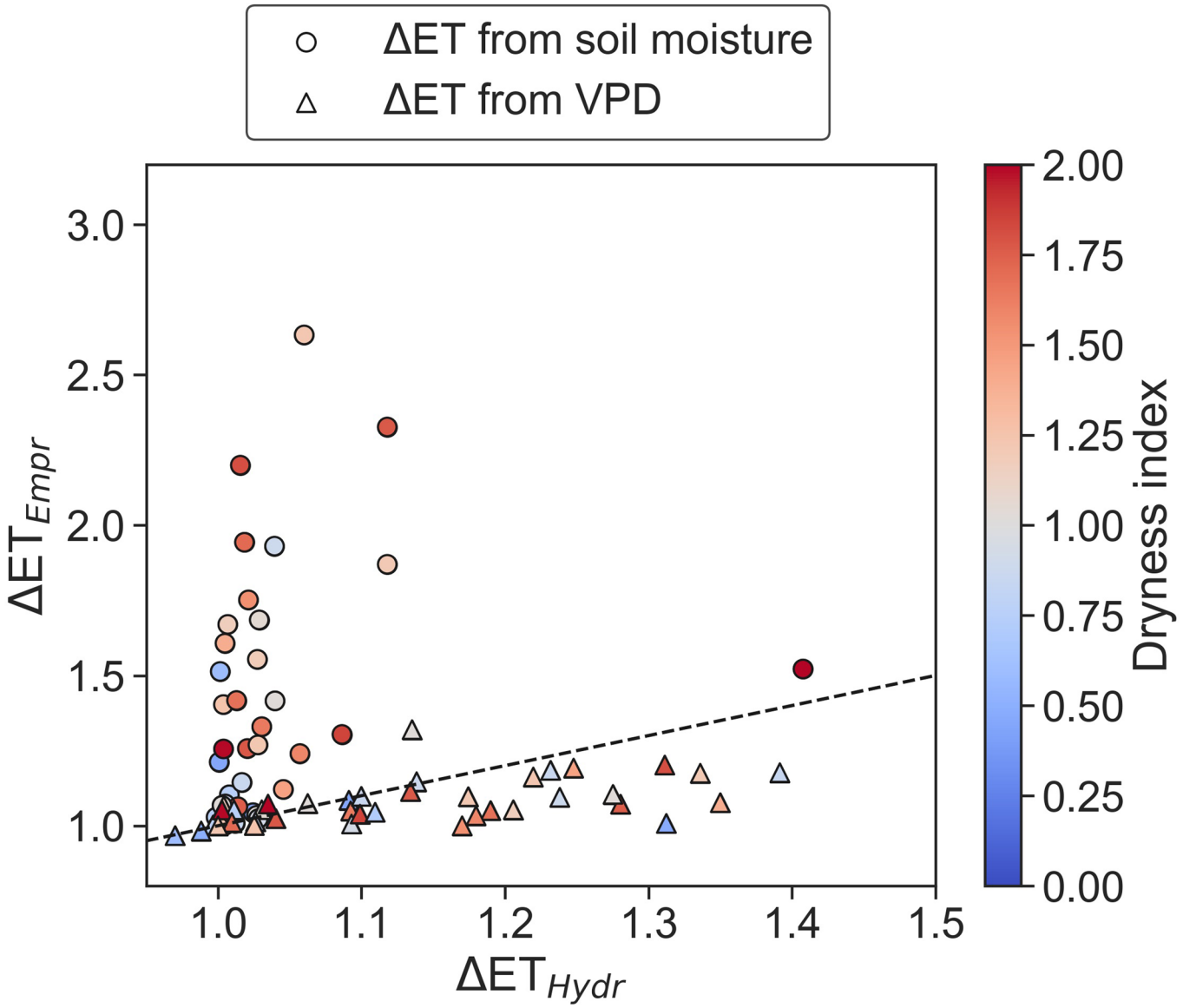

Extended Data Fig. 6 | Restriction effect of soil moisture and VPD on ET across sites with different dryness index. A replica of Fig. 3 (main text) but color-coded with dryness index. Dryness index is calculated as the ratio between long-term mean potential evapotranspiration and long-term mean precipitation. Circles and triangles represent soil moisture and VPD restricted ET, respectively.

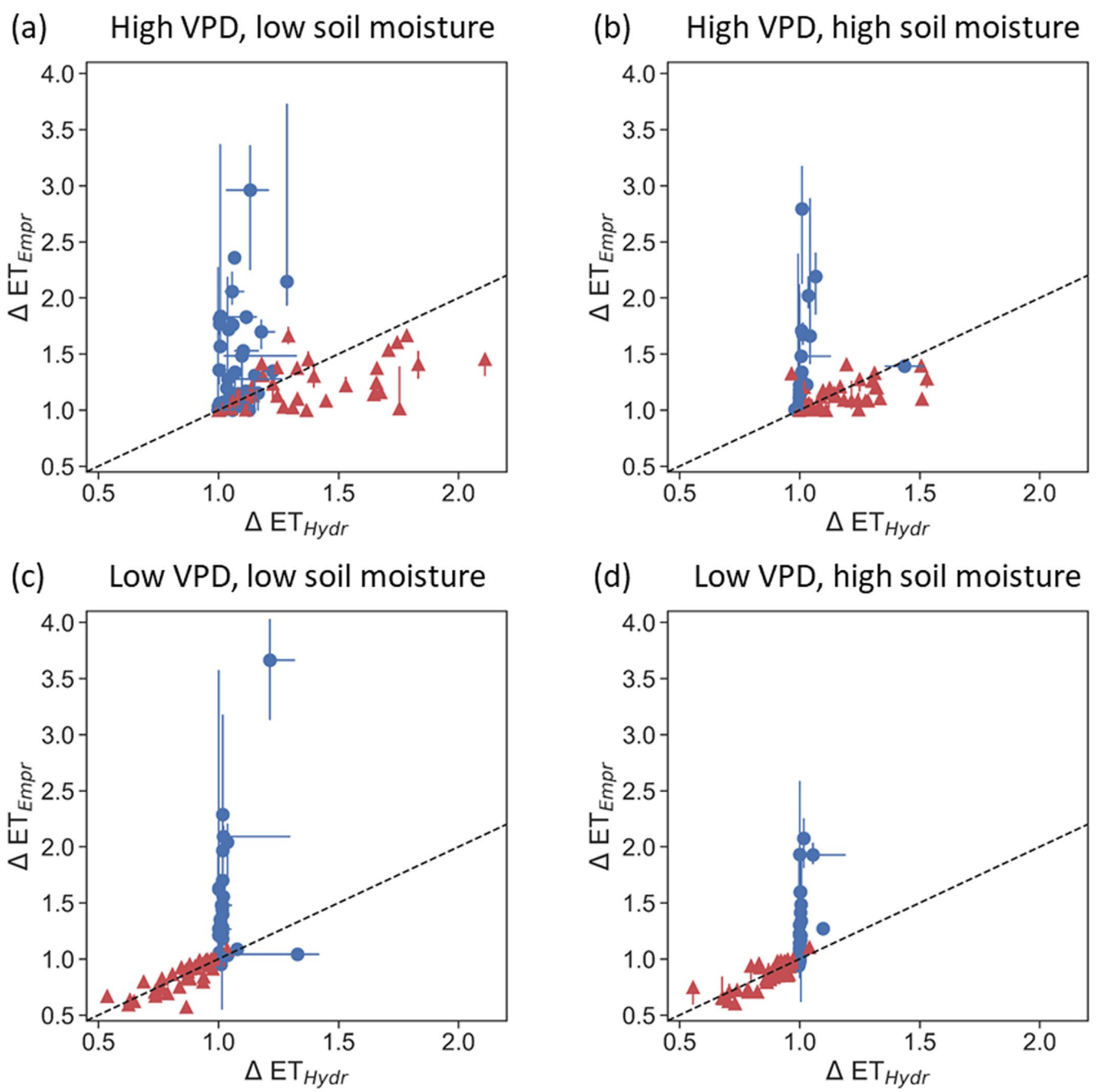

Extended Data Fig. 7 | Restriction effect of soil moisture and VPD on ET across sites during four sub-periods. The four sub-periods are the same as in Fig. 2 (main text), that is, **a**, high VPD low soil moisture; **b**, high VPD high soil moisture; **c**, low VPD low soil moisture; and **d**, low VPD high soil moisture. Symbols are the same as in Fig. 3 (main text).

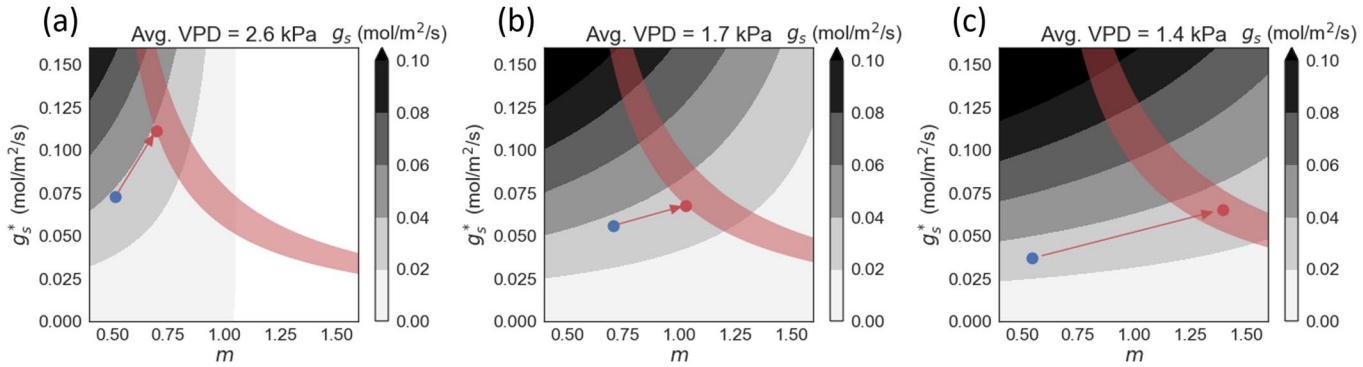

Extended Data Fig. 8 | Temporal average of the reference stomatal conductance (g_s^*) and the VPD-sensitivity (m) at a, AU-Wom, b, BE-Vie, and c, IT-Isp. Blue and red dots represent the estimates under a light-saturated condition using the empirical and hydraulic models, respectively. The red belts indicate the hydraulic constraint. Grey areas show the contours of stomatal conductance (g_s).

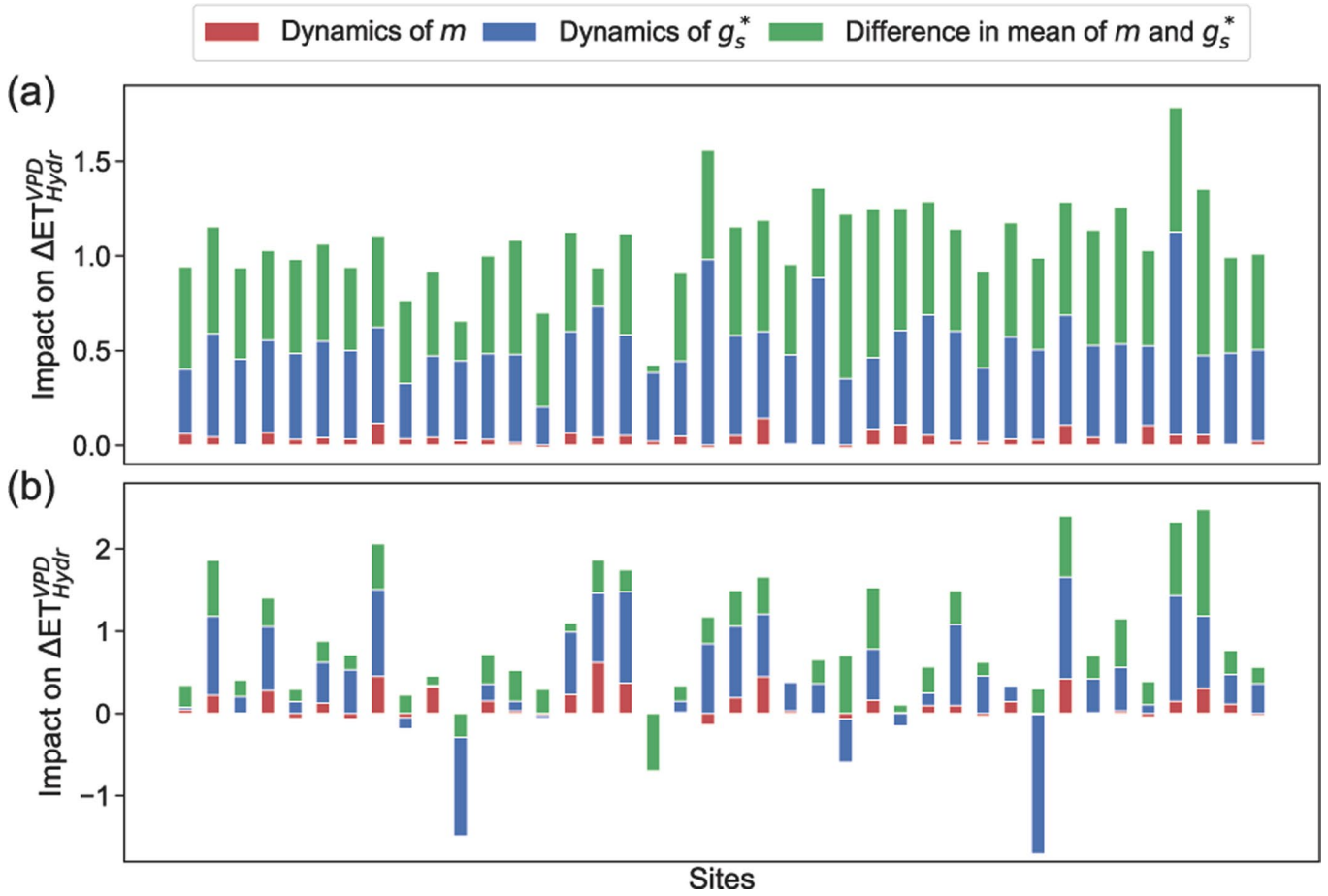

Extended Data Fig. 9 | Impact of the dynamics of the VPD sensitivity (*m*), the dynamics of the reference stomatal conductance g_s^*, and the difference in the mean of *m* and g_s^* on the restriction effect of VPD on ET estimated using the hydraulic model (ΔET_{Hydr}^{VPD}). The impacts averaged over **a**, the entire record period, and **b**, the stressed period, that is, when leaf water potential falls below its 75th percentile at each site, are plotted. Sites are listed from left to right in order of increasing dryness, as measured by the ratio of mean annual potential ET to mean annual precipitation.

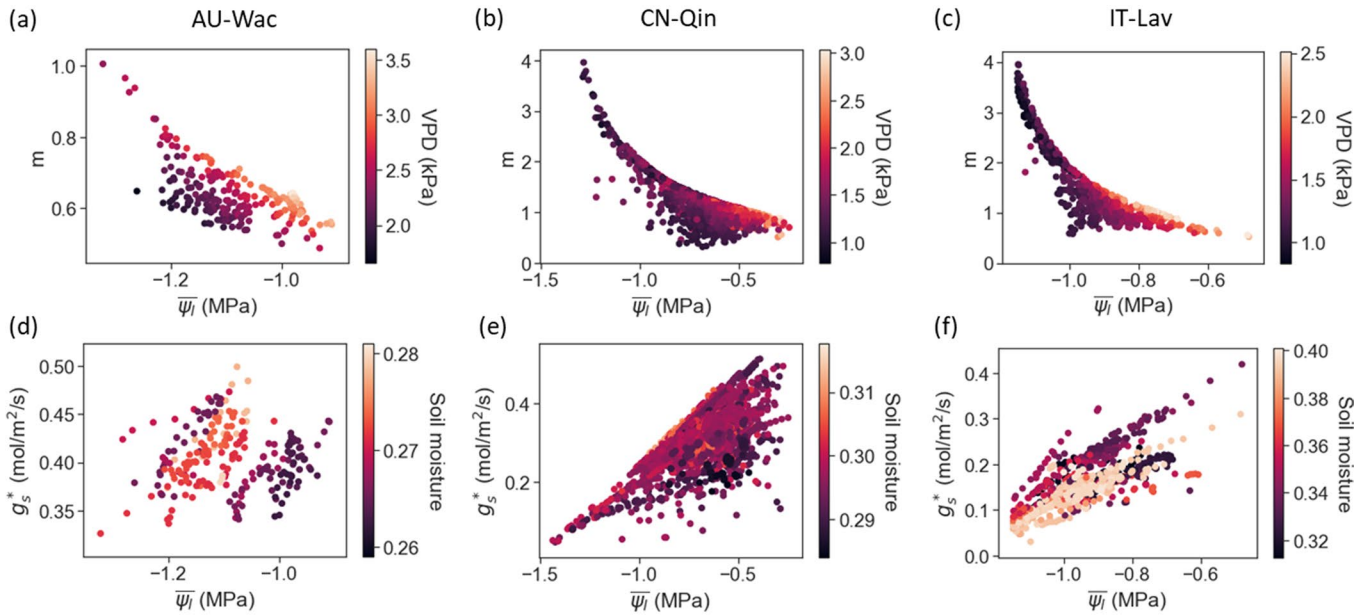

Extended Data Fig. 10 | Relation between the daily average leaf water potential ($\overline{\psi_l}$) and (a–c) the VPD sensitivity (m) of the hydraulic model and (d–f) the reference stomatal conductance (g_s^*) at three example sites. m was calculated using $(1 - g_s/g_s^*)/\ln(D)$ under light saturated conditions, where g_s and g_s^* were calculated using the full stomatal optimization model (equation (5) in Methods).